A Parallel Computational Model for Three-Dimensional, Thermo-Mechanical Stokes Flow Simulations of Glaciers and Ice Sheets

Wei Leng[1], Lili Ju[2,*], Max Gunzburger[3] and Stephen Price[4]

[1] *State Key Laboratory of Scientific and Engineering Computing, Chinese Academy of Sciences, Beijing 100190, China.*
[2] *Department of Mathematics, University of South Carolina, Columbia, SC 29208, USA.*
[3] *Department of Scientific Computing, Florida State University, Tallahassee, FL 32306, USA.*
[4] *Theoretical Division, Los Alamos National Laboratory, Los Alamos, NM 87545. USA.*

Abstract. This paper focuses on the development of an efficient, three-dimensional, thermo-mechanical, nonlinear-Stokes flow computational model for ice sheet simulation. The model is based on the parallel finite element model developed in [14] which features high-order accurate finite element discretizations on variable resolution grids. Here, we add an improved iterative solution method for treating the nonlinearity of the Stokes problem, a new high-order accurate finite element solver for the temperature equation, and a new conservative finite volume solver for handling mass conservation. The result is an accurate and efficient numerical model for thermo-mechanical glacier and ice-sheet simulations. We demonstrate the improved efficiency of the Stokes solver using the ISMIP-HOM Benchmark experiments and a realistic test case for the Greenland ice-sheet. We also apply our model to the EISMINT-II benchmark experiments and demonstrate stable thermo-mechanical ice sheet evolution on both structured and unstructured meshes. Notably, we find no evidence for the "cold spoke" instabilities observed for these same experiments when using finite difference, shallow-ice approximation models on structured grids.

Corresponding author. Email addresses: wleng@lsec.cc.ac.cn (W. Leng), ju@math.sc.edu (L. Ju), mgunzburger@fsu.edu (M. Gunzburger), sprice@lanl.gov (S. Price)

1   Introduction

During the past five years, there has been a concerted effort towards the development of improved numerical and computational models for glaciers and ice sheets. This is due to renewed concerns about the potential for future sea-level rise from land-ice melting [1–3] and to deficiencies in existing land-ice models, as highlighted by the last assessment report of the Intergovernmental Panel on Climate Change [32, 33]. A primary deficiency of the land-ice models used in that report was the simplified treatment of the ice-sheet dynamics which governs the three-dimensional velocity field within the ice. For glaciers and ice sheets, dynamical behavior is most completely and accurately described by a nonlinear Stokes system; recent papers [13, 14, 36] have reported the numerical and computational treatment of such models.

In [14], we reported on a new, nonlinear Stokes computational model, which used high-order accurate finite element methods on unstructured, variable resolution meshes. That work concentrated solely on the efficient and accurate parallel-computational solution of the Stokes momentum balance equations. Here, we mainly focus on important improvements in numerical approximations and solvers to that basically same computational model in order to make it more efficient and useful for practical science applications, in particular the simulation of large-scale, thermo-mechanically coupled ice-sheet evolution.

The remainder of this paper is organized as follows. In Section 2, we present the governing equations for ice-sheet dynamics and evolution of ice temperature and thickness in the Stokes thermo-mechanical model for simulating ice-sheet flow. Their numerical approximations and consequent solution techniques are then presented in Section 3. In Section 4, we test our computational model using standard diagnostic and prognostic experiments and compare our results with those from some previous models. Concluding remarks follow in Section 5.

2   The Stokes thermo-mechanical model for ice-sheet flow

The three-dimensional, thermo-mechanical Stokes ice-sheet model consists of three coupled components: the diagnostic, nonlinear Stokes equations governing the flow dynamics (conservation of momentum), the prognostic equation describing the evolution of the ice temperature, and the prognostic equation determining changes in the ice-sheet geometry (conservation of mass). See, e.g., [11,13,14,16,35,36], for additional details concerning the model we consider here.

Let $[0, t_{\max}]$ denote the time interval of interest and Ω_t the three-dimensional, time-varying spatial domain occupied by the ice sheet. The dynamic behavior of the ice-sheet is modeled by the Stokes equations for an incompressible, power-law viscous fluid in a

low-Reynolds number flow,

$$-\nabla \cdot \sigma = \rho \mathbf{g}, \qquad \text{in } [0, t_{\max}] \times \Omega_t, \tag{2.1a}$$

$$\nabla \cdot \mathbf{u} = 0, \qquad \text{in } [0, t_{\max}] \times \Omega_t, \tag{2.1b}$$

where $\mathbf{u} = (u, v, w)$ denotes the velocity vector, σ the stress tensor, ρ the (constant and uniform) ice density, and $\mathbf{g}$ the gravitational acceleration.[†]

The stress tensor can be split into a deviatoric part and an isotropic pressure as

$$\sigma = \tau - p\mathbf{I}, \tag{2.2}$$

where $p = -\frac{1}{3} trace(\sigma)$. The constitutive equation for ice links the deviatoric stress τ to the strain rate $\dot{\varepsilon}_{\mathbf{u}} = \frac{1}{2}(\nabla \mathbf{u} + \nabla \mathbf{u}^T)$ by Glen's flow law [19, 21], which can be written in Newtonian form as

$$\tau = 2\eta \dot{\varepsilon}_{\mathbf{u}}. \tag{2.3}$$

In (2.3), η denotes the strain-rate and temperature dependent effective viscosity coefficient defined by

$$\eta = \frac{1}{2} A^{-1/n} \epsilon_{\mathbf{u}}^{(1-n)/n}, \tag{2.4}$$

where n is usually taken as 3 for isotropic ice, A is the deformation rate factor, and $\epsilon_{\mathbf{u}}$ is the effective strain rate defined as

$$\epsilon_{\mathbf{u}} = \left(\frac{1}{2} \dot{\varepsilon}_{\mathbf{u}} : \dot{\varepsilon}_{\mathbf{u}}\right)^{1/2} = \left(\frac{1}{2}((\dot{\varepsilon}_{\mathbf{u}})_{11}^2 + (\dot{\varepsilon}_{\mathbf{u}})_{22}^2 + (\dot{\varepsilon}_{\mathbf{u}})_{33}^2) + (\dot{\varepsilon}_{\mathbf{u}})_{12}^2 + (\dot{\varepsilon}_{\mathbf{u}})_{23}^2 + (\dot{\varepsilon}_{\mathbf{u}})_{31}^2\right)^{1/2}. \tag{2.5}$$

The deformation rate factor A depends on the temperature and pressure, and possibly on other properties such as ice-crystal size and orientation and impurity content [21]. Following previous work [20], we assume that A depends only on temperature and obeys an Arrhenius relation defined by

$$A = A(T) = a \exp\left(\frac{-Q}{RT}\right), \tag{2.6}$$

where a is an empirical constant often used as a tuning parameter, Q denotes the activation energy, R the universal gas constant, and T the absolute temperature measured in degrees Kelvin.

The ice sheet domain Ω_t at time t is defined as

$$\Omega_t = \left\{ (x, y, z) \mid b(x, y) < z < s(x, y, t), \text{ for } (x, y) \in \Omega_H, t \in [0, t_{\max}] \right\},$$

where Ω_H denotes the horizontal domain of interest that covers the horizontal extent of the ice sheet, $s(x, y, t)$ defines the top surface elevation, and $b(x, y)$ defines the bed

---

[†]Note that because the ice velocity is small and temporal changes in the velocity are slower that those of the temperature, that, as is generally accepted, the inertial terms in the Navier-Stokes equations have been neglected to obtain (2.1a).

elevation. Here, $b(x,y)$ is assumed to be fixed with respect to time, i.e., neither isostatic rebound nor erosion are considered.

At the top surface of the ice-sheet Γ_s, we impose the stress continuity boundary condition

$$\sigma \cdot \mathbf{n} = -p_{atm} \cdot \mathbf{n} \qquad \text{on } \Gamma_s, \tag{2.7}$$

where $\mathbf{n}$ denotes the outer unit normal at the ice-sheet surface and p_{atm} the atmospheric pressure. Because atmospheric pressure is negligible relative to pressure within the ice column, we make the standard simplification that $p_{atm} = 0$ so that (2.7) reduces to a stress free boundary condition.

The bottom surface Γ_b of the ice-sheet can be decomposed into two parts, $\Gamma_{b,fix}$ at which the ice sheet is fixed to the bottom bedrock and $\Gamma_{b,sld}$ at which the ice sheet is allowed to slide; on both parts, a non-penetration condition on the velocity is applied. Specifically, on the fixed part of the basal boundary we apply a zero-velocity boundary condition

$$\mathbf{u} = \mathbf{0} \qquad \text{on } \Gamma_{b,fix} \tag{2.8}$$

and, on the sliding part, we apply a *Rayleigh friction* boundary condition

$$\mathbf{u} \cdot \mathbf{n} = 0 \quad \text{and} \quad \mathbf{n} \cdot \sigma \cdot \mathbf{t} = -\beta^2 \mathbf{u} \cdot \mathbf{t} \qquad \text{on } \Gamma_{b,sld}, \tag{2.9}$$

where β^2 is a given positive definite coefficient[‡] and $\mathbf{t}$ is any unit vector tangential to the bottom surface.

Along the lateral boundary Γ_ℓ, we impose for different settings one of three types of boundary conditions, depending on the physical domain boundary or benchmark domain boundary under consideration: a stress-free condition $\sigma \cdot \mathbf{n} = \mathbf{0}$ or a zero-velocity condition $\mathbf{u} = \mathbf{0}$ or periodic boundary conditions.

The governing equation for the temperature in the ice sheet is given by

$$\rho c \frac{\partial T}{\partial t} + \rho c \mathbf{u} \cdot \nabla T = \nabla \cdot (\kappa \nabla T) + 2\eta \dot{\varepsilon}_{\mathbf{u}} : \dot{\varepsilon}_{\mathbf{u}} \qquad \text{in } [0, t_{\max}] \times \Omega_t, \tag{2.10}$$

where c and κ denote the specific heat capacity and thermal conductivity of ice, respectively. These and the other thermal parameters used in our study are assumed to be independent of ice temperature because they are weak linear functions of temperature over the range expected in ice sheets. In (2.10), non-steady and advective changes in temperature (the first and second terms on the left-hand side, respectively) are balanced by temperature diffusion and internal strain rate heating (the first and second terms on the right-hand side, respectively).

The boundary conditions at the bottom and top surfaces Γ_b and Γ_s of the ice sheet are given by

$$\frac{\partial T}{\partial \mathbf{n}}\bigg|_{\Gamma_b} = -\frac{G}{\kappa} \qquad \text{and} \qquad T|_{\Gamma_s} = T_{\text{surf}}, \tag{2.11}$$

[‡]For realistic simulations, the value of β^2 may be vary in space and times, for example, as a function of the type of basal substrate, the presence, absence or pressure of subglacial water, etc.

where **n** is the outer unit normal on the ice sheet bottom surface, G is the geothermal heat flux along the bottom surface and T_{surf} is the mean annual temperature field along the top surface. Another possible source could be added to (2.11) is the heating at the bed due to friction which is given by the basal traction vector dotted with the basal sliding vector, but it is often negligible because essentially realistic ice-sheet flows are slow and the major water lubrication is largely controlled by Moulins.

If the ice temperature reaches the melting point, the ice sheet will melt down and leads to mass loss. However, for simplicity the melting model is not included here and the evolving temperature is assumed to be constrained so that it cannot exceed the pressure-melting temperature T' with

$$T' = T_0 - \gamma(s - z), \tag{2.12}$$

where γ is the Clausius-Clapeyron gradient which defines the melting point dependence on pressure.

The ice-sheet geometry evolution equation, derived from local mass-conservation, is given by

$$\frac{\partial H}{\partial t} = -\nabla \cdot (\overline{\mathbf{u}} H) + m \qquad \text{in } [0, t_{\max}] \times \Omega_H, \tag{2.13}$$

where $H = s - b$ denotes the ice thickness, $\overline{\mathbf{u}}$ is the vertically averaged velocity, and m denotes a source/sink term resulting from the ice sheet surface mass balance (i.e., climate driven accumulation or melting of ice) and basal mass balance (i.e., melting or freezing of ice at the ice-bedrock interface).

Table 1 lists the values of the physical constants and parameters used in the computational experiments.

Table 1: Model parameters and physical constants used in the experiments of the Stokes ice-sheet model.

Symbol	Constant	Value	Unit
ρ	Density of ice	910	kgm^{-3}
g	Acceleration due to gravity	9.81	ms^{-2}
n	Power in Glen's law	3	-
T_0	Triple point of water	273.15	K
G	Geothermal heat flux	4.2×10^{-2}	Wm^{-2}
k	Thermal conductivity of ice	2.1	$\text{Wm}^{-1}\text{K}^{-1}$
c	Specific heat capacity of ice	2009	$\text{Jkg}^{-1}\text{K}^{-1}$
γ	Clausius-Clapeyron gradient	8.66×10^{-4}	K m^{-1}
a	Tuning parameter	3.61×10^{-13} if $T < 263.15\text{K}$	$\text{Pa}^{-3}\text{s}^{-1}$
		1.73×10^{-13} if $T \geq 263.15\text{K}$	
Q	Activation energy	6.0×10^4 if $T < 263.15\text{K}$	Jmol^{-1}
		13.9×10^4 if $T \geq 263.15\text{K}$	
R	Gas constant	8.314	$\text{Jmol}^{-1}\text{K}^{-1}$
	Seconds per year	31556926	

3 Numerical discretizations and solution techniques

3.1 The Picard-Newton finite element Stokes solver for ice-sheet dynamics

Let $\mathcal{T}_h$ denote a three-dimensional layered tetrahedral triangulation of the ice-sheet domain Ω_t; in particular, we use the grids described in [14]. Let $P_{1,h}(\mathcal{T}_h)$ and $P_{2,h}(\mathcal{T}_h)$ denote the continuous piecewise-linear and quadratic polynomial finite element spaces (also called the Taylor-Hood element pair), respectively, defined with respect to the tetrahedral grid. Define $\widetilde{\mathbf{P}}_{2,h}$ as

$$\widetilde{\mathbf{P}}_{2,h}(\mathcal{T}_h) = \left\{ \mathbf{u}_h \in (P_{2,h}(\mathcal{T}_h))^3 \mid \mathbf{u}_h|_{\Gamma_l \cup \Gamma_{b,fix}} = 0, \ (\mathbf{u}_h \cdot \mathbf{n})|_{\Gamma_{b,sld}} = 0 \right\}. \tag{3.1}$$

Then, a finite element discretization of the Stokes problem is defined as follows: given Ω_t and $\mathcal{T}_h$, seek $\mathbf{u}_h \in \widetilde{\mathbf{P}}_{2,h}(\mathcal{T}_h)$ and $p_h \in P_{1,h}(\mathcal{T}_h)$ such that

$$\begin{cases} \displaystyle\int_{\Omega_t} 2\eta_{\mathbf{u}_h} \dot{\boldsymbol{\varepsilon}}_{\mathbf{u}_h} : \dot{\boldsymbol{\varepsilon}}_{\mathbf{v}_h} \, d\mathbf{x} + \int_{\Gamma_{b,sld}} \beta^2 \mathbf{u}_h \cdot \mathbf{v}_h \, ds - \int_{\Omega_t} p_h \nabla \cdot \mathbf{v}_h \, d\mathbf{x} = \rho \int_{\Omega_t} \mathbf{g} \cdot \mathbf{v}_h \, d\mathbf{x}, \\ \displaystyle -\int_{\Omega_t} q_h \nabla \cdot \mathbf{u}_h \, d\mathbf{x} = 0, \end{cases} \tag{3.2}$$

for all test functions $\mathbf{v}_h \in \widetilde{\mathbf{P}}_{2,h}(\mathcal{T}_h)$ and $q_h \in P_{1,h}(\mathcal{T}_h)$. Due to the dependence of η on the approximate velocity $\mathbf{u}_h$, (3.2) is a nonlinear system of equations for the approximate velocity $\mathbf{u}_h$ and approximate pressure p_h.

We use a hybrid Picard-Newton iterative algorithm to solve the nonlinear system (3.2). The Picard iteration is robust with respect to the initial guess for the solution, but is at best linearly convergent for solving the nonlinear finite element Stokes system. Thus, it is time consuming for long-time and large-spatial scale simulations in practical applications, such as decades to century scale, whole-ice sheet simulations of Greenland and Antarctica. Newton-based nonlinear iterative solvers are putatively quadratically convergent but are much less robust with respect to the initial solution guess. Our approach is to first run the Picard iteration for a few steps to provide a good initial guess for the Newton iteration, which then takes over until the solution converges. This hybrid approach provides a powerful and efficient tool for solving the nonlinear Stokes system.

The Picard iteration simply lags the velocity-dependent viscosity $\eta_{\mathbf{u}_h}$ in (3.2), i.e., at any nonlinear iteration, $\eta_{\mathbf{u}_h}$ is evaluated using the approximate velocity solution obtained at the end of the previous nonlinear iteration. Thus, starting with an initial guess $\mathbf{u}_h^{(0)}$ for the velocity (which is often taken to be $\mathbf{u}_h^{(0)} = \mathbf{0}$ in which case $\eta_{\mathbf{u}_h^0}$ is set to be a certain positive constant), we have for $j = 1, 2, \cdots$, that $\mathbf{u}_h^{(j)}$ and $p_h^{(j)}$ are determined by solving the *linear* system of algebraic equations

$$\begin{cases} \displaystyle\int_{\Omega_t} 2\eta_{\mathbf{u}_h^{(j-1)}} \dot{\boldsymbol{\varepsilon}}_{\mathbf{u}_h^{(j)}} : \dot{\boldsymbol{\varepsilon}}_{\mathbf{v}_h} \, d\mathbf{x} + \int_{\Gamma_{b,sld}} \beta^2 \mathbf{u}_h^{(j)} \cdot \mathbf{v}_h \, ds - \int_{\Omega_t} p_h^{(j)} \nabla \cdot \mathbf{v}_h \, d\mathbf{x} = \rho \int_{\Omega_t} \mathbf{g} \cdot \mathbf{v}_h \, d\mathbf{x}, \\ \displaystyle -\int_{\Omega_t} q_h \nabla \cdot \mathbf{u}_h^{(j)} \, d\mathbf{x} = 0. \end{cases} \tag{3.3}$$

Newton's method requires computation of both the residual and the Jacobian of the nonlinear system (3.2). Because the nonlinear term of (3.2) arises from the term $\int_{\Omega_t} \boldsymbol{\tau}_{\mathbf{u}_h} : \dot{\boldsymbol{\varepsilon}}_{\mathbf{v}_h} d\mathbf{x}$ with $\boldsymbol{\tau}_{\mathbf{u}_h} = 2\eta_{\mathbf{u}_h} \dot{\boldsymbol{\varepsilon}}_{\mathbf{u}_h}$, we only need compute the Jacobian of this term. Let $\delta(f(\mathbf{u}))$ denotes the change of $f(\mathbf{u})$ with respect to $\delta\mathbf{u}$ (the change of $\mathbf{u}$). We then find that

$$
\begin{aligned}
\delta(\boldsymbol{\tau}_{\mathbf{u}}) &= \delta\left(A^{-1/3} \epsilon_{\mathbf{u}}^{-2/3} \dot{\boldsymbol{\varepsilon}}_{\mathbf{u}} \right) \\
&= A^{-1/3} \left(\epsilon_{\mathbf{u}}^{-2/3} \delta(\dot{\boldsymbol{\varepsilon}}_{\mathbf{u}}) + \dot{\boldsymbol{\varepsilon}}_{\mathbf{u}} \delta(\epsilon_{\mathbf{u}}^{-2/3}) \right)
\end{aligned}
\tag{3.4}
$$

and

$$
\begin{aligned}
\delta(\epsilon_{\mathbf{u}}^{-2/3}) &= \delta\left(\left(\frac{1}{2}\dot{\boldsymbol{\varepsilon}}_{\mathbf{u}} : \dot{\boldsymbol{\varepsilon}}_{\mathbf{u}} \right)^{-1/3} \right) \\
&= -\frac{1}{3}\left(\frac{1}{2}\dot{\boldsymbol{\varepsilon}}_{\mathbf{u}} : \dot{\boldsymbol{\varepsilon}}_{\mathbf{u}} \right)^{-4/3} \left(\sum_{ij} (\dot{\boldsymbol{\varepsilon}}_{\mathbf{u}})_{ij} (\delta\dot{\boldsymbol{\varepsilon}}_{\mathbf{u}})_{ij} \right) \\
&= -\frac{1}{3} \epsilon_{\mathbf{u}}^{-2/3} \epsilon_{\mathbf{u}}^{-2} \left(\sum_{ij} (\dot{\boldsymbol{\varepsilon}}_{\mathbf{u}})_{ij} (\delta\dot{\boldsymbol{\varepsilon}}_{\mathbf{u}})_{ij} \right).
\end{aligned}
\tag{3.5}
$$

Consequently we have

$$
\delta(\boldsymbol{\tau}_{\mathbf{u}}) = A^{-1/3} \epsilon_{\mathbf{u}}^{-2/3} \left(\delta(\dot{\boldsymbol{\varepsilon}}_{\mathbf{u}}) - \frac{2}{3} \frac{1}{(2\epsilon_{\mathbf{u}}^2)} \left(\sum_{ij} (\dot{\boldsymbol{\varepsilon}}_{\mathbf{u}})_{ij} (\delta\dot{\boldsymbol{\varepsilon}}_{\mathbf{u}})_{ij} \right) \dot{\boldsymbol{\varepsilon}}_{\mathbf{u}} \right)
\tag{3.6}
$$

and the Jacobian of $\int_{\Omega_t} \boldsymbol{\tau}_{\mathbf{u}} : \dot{\boldsymbol{\varepsilon}}_{\mathbf{v}} d\mathbf{x}$ is given by

$$
\int_{\Omega_t} A^{-1/3} \epsilon_{\mathbf{u}}^{-2/3} \left(\frac{\delta\dot{\boldsymbol{\varepsilon}}_{\mathbf{u}}}{\delta\mathbf{u}} - \frac{2}{3} \frac{1}{(2\epsilon_{\mathbf{u}}^2)} \left(\sum_{ij} (\dot{\boldsymbol{\varepsilon}}_{\mathbf{u}})_{ij} \frac{(\delta\dot{\boldsymbol{\varepsilon}}_{\mathbf{u}})_{ij}}{\delta\mathbf{u}} \right) \dot{\boldsymbol{\varepsilon}}_{\mathbf{u}} \right) : \dot{\boldsymbol{\varepsilon}}_{\mathbf{v}} d\mathbf{x}.
\tag{3.7}
$$

Thus, the variational problem for the Newton method is to seek $\delta\mathbf{u}_h \in \widetilde{\mathbf{P}}_{2,h}(\mathcal{T}_h)$ and $\delta p_h \in P_{1,h}(\mathcal{T}_h)$ such that

$$
\begin{cases}
\displaystyle \int_{\Omega_t} A^{-1/3} \epsilon_{\mathbf{u}_h^{(j-1)}}^{-2/3} \left(\dot{\boldsymbol{\varepsilon}}_{\delta\mathbf{u}_h} - \frac{2}{3} \frac{1}{\left(2\epsilon_{\mathbf{u}_h^{(j-1)}}^2\right)} \left(\dot{\boldsymbol{\varepsilon}}_{\delta\mathbf{u}_h} : \dot{\boldsymbol{\varepsilon}}_{\mathbf{u}_h^{(j-1)}} \right) \dot{\boldsymbol{\varepsilon}}_{\mathbf{u}_h^{(j-1)}} \right) : \dot{\boldsymbol{\varepsilon}}_{\mathbf{v}_h} d\mathbf{x} \\[4mm]
\qquad\qquad + \displaystyle \int_{\Gamma_{b,sld}} \beta^2 \delta\mathbf{u}_h \cdot \mathbf{v}_h \, ds - \int_{\Omega_t} \delta p_h \nabla \cdot \mathbf{v}_h \, d\mathbf{x} = -\mathrm{Res}_{\mathbf{u}}^{(j-1)}, \\[4mm]
-\displaystyle \int_{\Omega_t} q_h \nabla \cdot \delta\mathbf{u}_h \, d\mathbf{x} = -\mathrm{Res}_p^{(j-1)},
\end{cases}
\tag{3.8}
$$

for all $\mathbf{v}_h \in \widetilde{\mathbf{P}}_{2,h}(\mathcal{T}_h)$ and $q_h \in P_{1,h}(\mathcal{T}_h)$, where $\mathrm{Res}_{\mathbf{u}}^{(j-1)}$ and $\mathrm{Res}_p^{(j-1)}$ are the residuals of (3.2) for the approximations $\mathbf{u}_h^{(j-1)}$ and $p_h^{(j-1)}$, respectively. Given the solution of (3.8), the

approximate solution at the jth step of the Newton method is given by $\mathbf{u}_h^{(j)} = \mathbf{u}_h^{(j-1)} + \delta\mathbf{u}_h$ and $p_h^{(j)} = p_h^{(j-1)} + \delta p_h$.

The diffusion part of the variational problem (3.8) is still coercive if the viscosity from the last step, $\epsilon_{\mathbf{u}_h^{(j-1)}}$, has an upper bound on Ω_t. We can show this by setting $\mathbf{v}_h = \delta\mathbf{u}_h = \mathbf{w}$, and use the Cauchy-Schwarz inequality to obtain

$$
\int_{\Omega_t} A^{-1/3} \epsilon_{\mathbf{u}_h^{(j-1)}}^{-2/3} \left(\dot{\boldsymbol{\varepsilon}}_{\mathbf{w}} - \frac{2}{3} \frac{1}{\left(2\epsilon_{\mathbf{u}_h^{(j-1)}}^2\right)} (\dot{\boldsymbol{\varepsilon}}_{\mathbf{w}} : \dot{\boldsymbol{\varepsilon}}_{\mathbf{u}_h^{(j-1)}}) \dot{\boldsymbol{\varepsilon}}_{\mathbf{u}_h^{(j-1)}} \right) : \dot{\boldsymbol{\varepsilon}}_{\mathbf{w}} \, d\mathbf{x}
$$

$$
= \int_{\Omega_t} A^{-1/3} \epsilon_{\mathbf{u}_h^{(j-1)}}^{-2/3} \left(\dot{\boldsymbol{\varepsilon}}_{\mathbf{w}} : \dot{\boldsymbol{\varepsilon}}_{\mathbf{w}} - \frac{2}{3} \frac{1}{\left(2\epsilon_{\mathbf{u}_h^{(j-1)}}^2\right)} (\dot{\boldsymbol{\varepsilon}}_{\mathbf{u}_h^{(j-1)}} : \dot{\boldsymbol{\varepsilon}}_{\mathbf{w}})^2 \right) d\mathbf{x}
$$

$$
\geq \int_{\Omega_t} A^{-1/3} \epsilon_{\mathbf{u}_h^{(j-1)}}^{-2/3} \left(\dot{\boldsymbol{\varepsilon}}_{\mathbf{w}} : \dot{\boldsymbol{\varepsilon}}_{\mathbf{w}} - \frac{2}{3} \frac{\left(2\epsilon_{\mathbf{u}_h^{(j-1)}}^2\right)}{\left(2\epsilon_{\mathbf{u}_h^{(j-1)}}^2\right)} (\dot{\boldsymbol{\varepsilon}}_{\mathbf{w}} : \dot{\boldsymbol{\varepsilon}}_{\mathbf{w}}) \right) d\mathbf{x}
$$

$$
= \frac{1}{3} \int_{\Omega_t} A^{-1/3} \epsilon_{\mathbf{u}_h^{(j-1)}}^{-2/3} (\dot{\boldsymbol{\varepsilon}}_{\mathbf{w}} : \dot{\boldsymbol{\varepsilon}}_{\mathbf{w}}) \, d\mathbf{x}
$$

$$
\geq c \|\mathbf{w}\|_{1,\Omega_t} \tag{3.9}
$$

for some constant $c > 0$.

Both the Picard and Newton methods produce, at each step, the linear finite element problems (3.3) and (3.8), respectively, which are symmetric saddle-point problems. The development of an efficient linear solver for such algebraic systems is described in [14], a block preconditioner is constructed to precondition the FGMRES iteration, and the sub-problem for the velocity in the block preconditioner is approximately solved by the algebraic multi-grid method.

3.2 The finite element ice-sheet temperature evolution solver

When solving the temperature equation (2.10), which is a typical advection-diffusion problem, a few difficulties arise. For example, (i) the problem is advection-dominated in the horizontal directions and (ii) the melting point constraint (2.12) needs to be satisfied throughout the three-dimensional temperature field. We use the SUPG-FEM (Streamline Upwind Petrov-Galerkin Finite Element Method) [6] to stabilize the numerical scheme.

A weak formulation of (2.10) is defined as follows: seek $T_h \in P_{3,h}(\mathcal{T}_h)$ satisfying $T_h|_{\Gamma_s} = T_{\text{surf},h}$

$$
\int_{\Omega_t} \left(\rho c \frac{\partial T_h}{\partial t} \phi_h + \rho c \mathbf{u}_h \cdot \nabla T_h \phi_h + \kappa \nabla T_h \cdot \nabla \phi_h + \mu \rho c (\mathbf{u}_h \cdot \nabla T_h)(\mathbf{u}_h \cdot \nabla \phi_h) \right) d\mathbf{x}
$$

$$
= \int_{\Omega_t} 2\eta_{\mathbf{u}_h, T_h} \dot{\boldsymbol{\varepsilon}}_{\mathbf{u}_h} : \dot{\boldsymbol{\varepsilon}}_{\mathbf{u}_h} \phi_h \, d\mathbf{x} \tag{3.10}
$$

for all test functions $\phi_h \in P_{3,h}(\mathcal{T}_h)$ and $\phi_h|_{\Gamma_s} = 0$, where $T_{\text{surf},h}$ is an approximation, e.g., an interpolant, of the given surface temperature field T_{surf} and the stabilization parameter μ is set to be $\mu = h/(2\|\mathbf{u}_h\|)$ with h chosen locally as the diameter of the tetrahedron and $\|\mathbf{u}_h\|$ the L^2 norm with respect to the tetrahedron. We use cubic finite element temperature approximations here because we found that, for the same cost (i.e., for the same number of degrees of freedom), quadratic approximations sometimes yield noticeable poorer results, e.g., they display numerical oscillations at the bottom of ice sheet in some of the tests presented in Section 4. Note this was not the case for velocity approximations for which quadratic approximations are entirely reliable. The melting point constraint (2.12) is treated using the nonlinear iterative method given in [36].

3.3   The finite volume ice-sheet thickness evolution solver

Let $\mathcal{Q}_H$ denote the two-dimensional triangulation of the horizontal extent Ω_H of the ice-sheet. For each vertex v_i of $\mathcal{Q}_H$, we build a patch around v_i by combining all triangles that have v_i as a vertex, then extend the two-dimensional patch in the vertical direction to create a volumetric patch P_i in the tetrahedral mesh $\mathcal{T}_h$. Then, the explicit, vertex-based finite volume scheme for updating the ice thickness is given by

$$\frac{(H_i^{n+1} - H_i^n)S_i}{\Delta t} = \sum_j F_j^n + m_i S_i, \tag{3.11}$$

where H_i^n denotes the ice thickness at the vertex v_i at time t^n, $\{F_j^n\}$ is the set of fluxes at all lateral faces of the control volume P_i, and S_i is the horizontal area of P_i. The flux F^n is upwinded to stabilize the scheme in space; specifically, we have

$$F_j^n = \begin{cases} \overline{\mathbf{u}}_j \cdot \mathbf{n}_j l_j H_j^- & \text{if } \overline{\mathbf{u}}_j \cdot \mathbf{n}_j > 0, \\ \overline{\mathbf{u}}_j \cdot \mathbf{n}_j l_j H_j^+ & \text{otherwise,} \end{cases} \tag{3.12}$$

where $\mathbf{n}_j$ is the outer normal unit vector on the jth lateral face of the control volume P_i, l_j is the horizontal length of the j-th lateral face, H_j^- is the average height inside the control volume, and H_j^+ is the average height in the neighboring control volume of the jth lateral face. The boundary condition for the scheme (3.11) is that the flux at the lateral faces of the domain is zero because the 2D extent of the ice sheet does not reach beyond the 2D computational domain.

   The scheme (3.11) updates the thickness of each point in map view using the explicit, forward Euler method, in which case an advective CFL condition must be satisfied for stability. This scheme is usually first-order accurate in both space and time, however, it exactly conserves the mass of the ice-sheet locally and globally which is very important to simulation of long-time ice-sheet evolution.

4 Numerical experiments

Parallel implementation of all numerical solvers for the above three-dimensional Stokes ice-sheet model use MPI (Message Passing Interface) based on domain decomposition methods discussed in [14].

4.1 Tests of the Stokes ice dynamics solver

We first test the performance of the Stokes ice dynamics solver, which is the core component of the proposed computational ice-sheet flow model.

4.1.1 The ISMIP-HOM benchmark experiments

The ISMIP-HOM benchmark experiments [23] focus on the solution of the diagnostic, three-dimensional flow field within an idealized, predominantly rectangular slab of ice with length L and average thickness 1 km, resting on a sloping surface. Lateral boundary conditions are either singly or doubly periodic and basal boundary conditions include both no slip and a periodic, specified pattern of the basal traction parameter β^2 in (2.9). Exps. A and B have a zero-velocity Dirichlet boundary condition on the basal surface Γ_b, whereas Exps. C and D include a *Rayleigh friction* basal sliding boundary condition (see [23] for more details). The application of our pure Picard-based Stokes solver to these tests was described in [14]. Here, we conduct Exps. A-D on a $40 \times 40 \times 20$ structured tetrahedral grid (192,000 tetrahedral elements and 827,604 degrees of freedom), primarily for the purpose of comparing performance between the Picard and hybrid Picard-Newton nonlinear iteration schemes. As expected, the simulated velocity and pressure agree very well with the results from [14] in all four experiments. Convergence behavior for the two methods for Exps. A and C are shown in Fig. 1. Exps. B and D show similar convergence behavior.

After starting with several Picard iterations, the Newton method converges quadratically in every case. The Picard-Newton method generally takes 8-15 iterations to reduce the relative residual by 10^{-10}, whereas the pure Picard method almost always took 20-25 iterations to reach a much larger relative residual of 10^{-4}. Note that the relative residual of the second iteration is used as the initial relative residual because we use a constant viscosity as the initial guess for the first iteration.

The Newton method is usually invoked at the fourth nonlinear iteration in each experiment. However, for the 5 km test cases, it is started between the 6-8th iteration in order to ensure convergence. This reflects the fact that nonlinear Stokes system is more difficult to converge as the aspect ratio of the domain (ratio of thickness to length) approaches 1 and/or as horizontal stress gradients start to make up a significant fraction of the momentum balance.
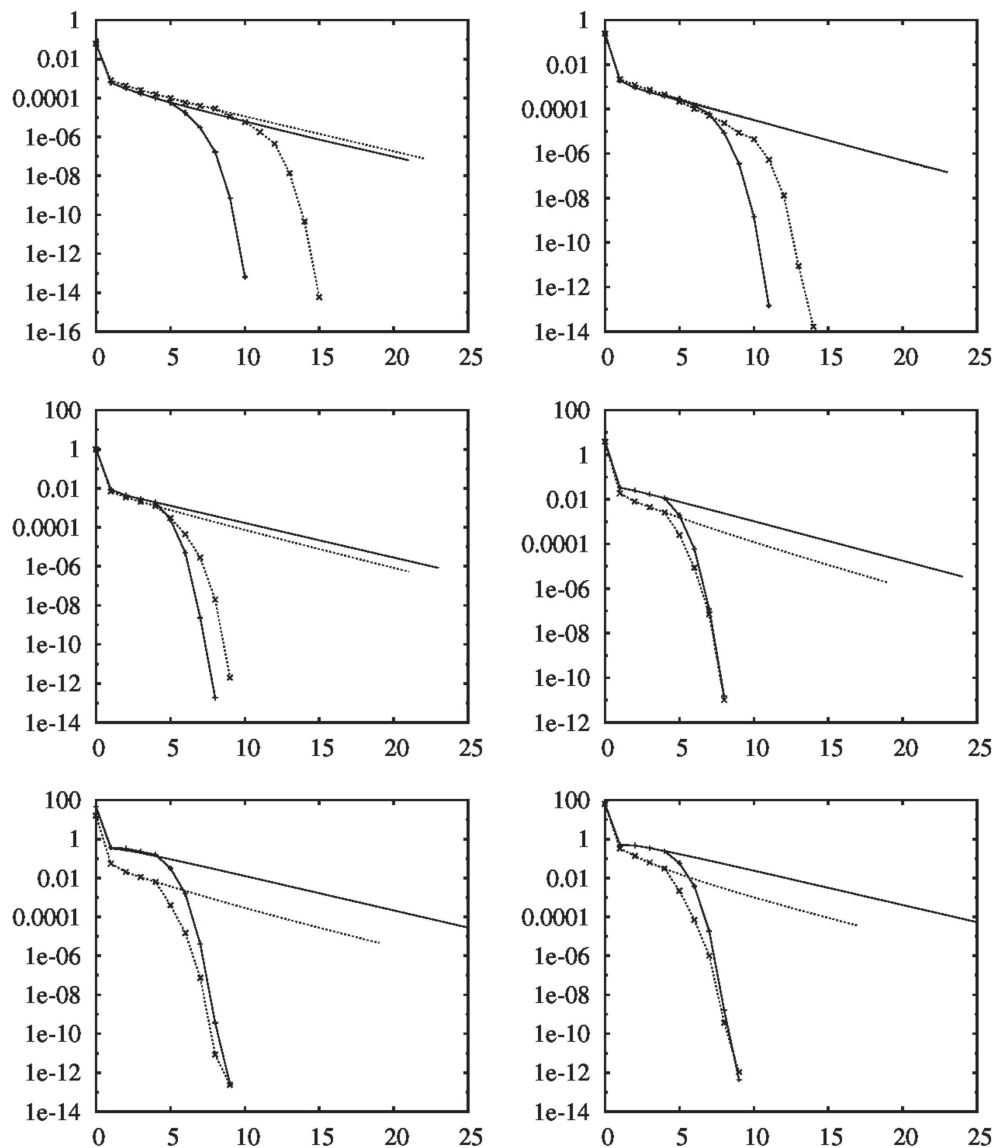
Figure 1: Convergence results of the pure Picard and Picard-Newton methods for ISMIP-HOM benchmark experiment A and C. From left to right and then from top to bottom: the ice-sheet horizontal length $L=$ 5km, 10km, 20km, 40km, 80km, 160km. Solid lines: Exp. A with pure Picard method. Solid lines with asterisk: Exp. A with Picard-Newton method. Dashed lines: Exp. C with pure Picard method. Dashed lines with plus: Exp. C with Picard-Newton method.

4.1.2 Realistic geometry and boundary conditions: Greenland ice sheet

Next, we test the performance of our computational model for a large-scale problem in which the ice sheet geometry and boundary conditions are quasi-realistic and similar to those that would be applied in practical climate science applications. The geometry and
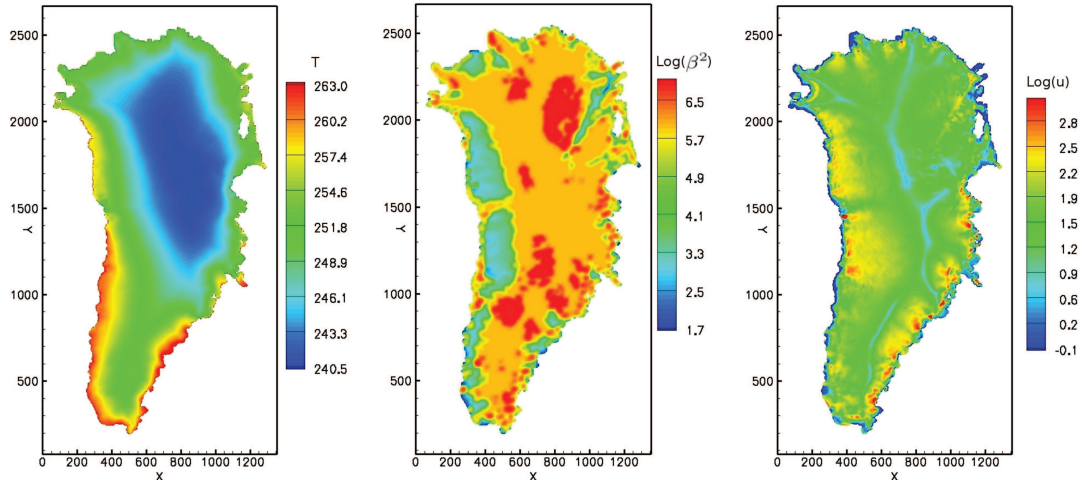
Figure 2: Greenland ice-sheet experiment model inputs and results. Left: the surface temperature (K); middle: the logarithm of the basal sliding parameter β^2 (Pa m^{-1}) along the bottom surface; right: the surface ice velocity magnitude (log base 10 of ma^{-1}).

surface temperature fields are for the Greenland ice sheet and are taken from the *SeaRISE* experiments (`http://www.azimuthproject.org/azimuth/show/SeaRISE`). At the top surface, we use the temperature field shown in Fig. 2-left; the temperature at the bottom is set to the local pressure-dependent melting temperature. The temperature inside the ice sheet is then vertically linearly interpolated between the top and basal surface values. This temperature field is then used to compute the flow rate factor A given in (2.6). We apply the sliding condition in (2.9) over the entire base of the ice sheet, i.e., $\Gamma_b = \Gamma_{b,sld}$. The basal friction parameter β^2 in the basal boundary condition (2.9), shown in Fig. 2-middle, is taken from the tuned initial condition of a previous large-scale Greenland simulation [28]. Note that in regions where β^2 is very large, the effect is equivalent to a no-slip basal boundary condition. For simplicity, we impose a zero-velocity condition on the lateral boundaries. This experiment is diagnostic: given the temperature field, geometry, and boundary conditions, the three-dimensional velocity field for the ice sheet is computed. A 5km resolution, structured, two-dimensional triangular mesh is generated to cover the Greenland ice-sheet horizontal domain Ω_H. From this, a 10-layer three-dimensional tetrahedral grid is constructed. The resulting three-dimensional grid has 730,675 vertices and about 3.9 million tetrahedral elements, giving a total of about 17 million degrees of freedom.

We first run 15 Picard iterations due to the irregular bottom bedrock topography, and then continue with Newton iterations until the change of velocity reduces to 10^{-4} ma^{-1} (meters per year). Note that we have changed the convergence criteria and convergence threshold from those in Section 4.1.1. The reason for these changes are that ISMIP-HOM experiments are used to demonstrate properties of our nonlinear iteration algorithm so

that the residual value and a small threshold is used, whereas for the more realistic examples involving the EISMINT experiments and the Greenland geometry, we do not need to converge to a 10^{-8} relative error; a sufficiently small change in the velocity is enough. The velocity change is an absolute value with unit ma^{-1}. For the Greenland example, 20 iterations (15 Picard + 5 Newton) are needed to meet the 10^{-4}ma^{-1} threshold. Using 256 processors, the calculation took about 30 minutes.[§] The results of the simulation are shown in Fig. 2-right. The modeled surface speeds in the ice-sheet interior are of the order of 10-100 ma^{-1}; in localized regions near the margins (i.e., bedrock troughs containing outlet glaciers), they are as large as 1000 ma^{-1}. These modeled speeds are broadly consistent with observed ice speeds and are largely the result of localized regions where rapid basal slip occurs (the blue and green regions in Fig. 2-middle).

4.2 EISMINT-II benchmark experiments for thermo-mechanically coupled ice-sheet evolution

The European Ice-Sheet Modeling Initiative (EISMINT) consists of a series of idealized prognostic experiments for studying the behavior of models designed to simulate ice-sheet evolution. The second phase of that set of experiments, EISMINT II [25], focussed on thermo-mechanically coupled ice-flow evolution. Importantly, at that time, the operational ice-sheet models taking part in the intercomparison project were all based on the Shallow-Ice Approximation (SIA). Those experiments assumed a radially symmetric ice-sheet geometry and boundary conditions with radially symmetric and idealized climate forcing. While all SIA-based models tested showed considerable agreement in their predictions, symmetry was often broken and distinct, regularly spaced "cold-ice spokes" (see Fig. 5) appeared in certain experiments. Different models and different experiments displayed spokes with different characteristics.

The EISMINT-II experimental setup features a square domain [0, 1500km] × [0, 1500km], a prescribed surface mass balance and upper-surface temperature, and an initial ice-sheet geometry. Depending on the experiment, no slip or sliding basal boundary conditions are prescribed. Ice-sheet evolution is governed by the coupled ice dynamics, temperature, and thickness equations.

The ice accumulation rate $M(\text{ma}^{-1})$ is defined as a function of the horizontal coordinates x and y,

$$M(x,y) = \min\left[M_{\text{max}}, S_b(R_{\text{el}} - \sqrt{(x-x_{\text{summit}})^2 + (y-y_{\text{summit}})^2})\right], \tag{4.1}$$

where M_{max} denotes the maximum accumulation rate and S_b is the gradient in surface

---

[§]Note that in this section we only perform a single Stokes model calculation. In Section 4.2 where we treat experiments for which the Stokes dynamics model is coupled to the time-dependent temperature and thickness equations, multiple Stokes dynamics calculations are performed, one at each time step. Because solutions at previous time steps provide good starting guesses for the nonlinear solvers, the number of iterations needed and thus the timings for Stokes dynamics solutions are considerably smaller for all time steps compared to that needed for the initialization step.

mass balance with horizontal distance from the ice-sheet center. Note that inside the circle of radius R_{el}, centered at (x_{summit}, y_{summit}), $M > 0$ (accumulation) whereas outside that circle, we have $M < 0$ (ablation). The ice-sheet surface temperature T_{surf} measured in K is similarly defined as a function of x and y as

$$T_{surf}(x,y) = T_{min} + S_T \sqrt{(x - x_{summit})^2 + (y - y_{summit})^2}, \qquad (4.2)$$

where T_{min} is the minimum surface air temperature in the ice sheet interior, and S_T is the air-temperature gradient with respect to the horizontal distance from the ice-sheet center.

The parameters listed in Table 2 were used for the temperature surface boundary equation (4.2), the ablation equation (4.1), and the temperature rheology equation (2.6). We report on the results of six experiments that are briefly described in Table 3. Exp. A is a basic thermo-mechanically coupled run that builds an equilibrium ice sheet from zero initial thickness. The other five experiments either start with the equilibrium initial condition from Exp. A or start with zero ice, and change a few of the experimental input parameters in order to investigate idealized changes in climate forcing. In [25], the result of Exp. E is not shown because it provides trivial checks on model consistency, and so Exp. E is also skipped in our simulations.

Table 2: Parameters used for the EISMINT-II benchmark experiments.

M_{max}	$0.5\,\text{ma}^{-1}$
S_b	$10^{-2}\,\text{ma}^{-1}\text{km}^{-1}$
R_{el}	$450\,\text{km}$
T_{min}	$238.15\,\text{K}$
S_T	$1.67 \times 10^{-2}\,\text{Kkm}^{-1}$
x_{summit}	$750.0\,\text{km}$
y_{summit}	$750.0\,\text{km}$

Table 3: Brief summary of the EISMINT-II benchmark experiments.

Experiment	Descriptive comment	Initial Cond.
A	Basic thermo-mechanical run	Zero ice
B	Stepped 5K air-temperature warming	Exp. A
C	Stepped change in accumulation rate	Exp. A
D	Stepped change in equilibrium line altitude	Exp. A
F	Stepped 15K air-temperature cooling	Zero ice
G	Basal slip throughout	Zero ice

Multi-resolution meshing is used in our EISMINT-II simulations to reduce the computational costs of three-dimensional modeling. For all experiments, the ice thickness and velocity have much larger spatial gradients at the ice sheet margins relative to the interior. Thus, we use a relatively finer grid at and near the ice-sheet margins than in the
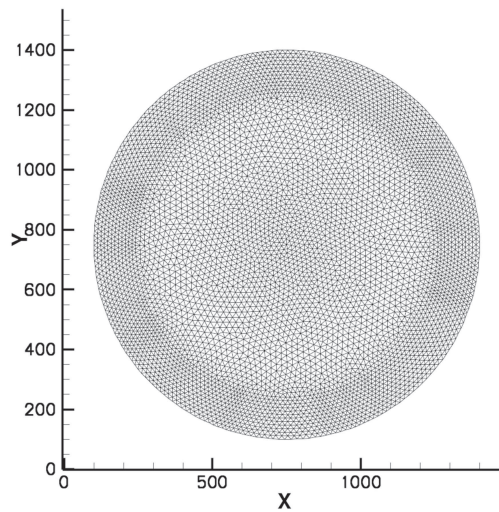
Figure 3: The triangular horizontal mesh from which our three-dimensional grid is constructed for the EISMINT-II benchmark experiments.

domain interior. The horizontal computational domain Ω_H we use is a circular region centered at (750 km, 750 km) with radius 650 km, which is enough to cover the region occupied by the ice during the entire ice-sheet evolution. The mesh is constructed in the following way. First, we generate a circular, two-dimensional, unstructured triangular mesh inside the computational domain under consideration using the package from [12]. Then, we further extend the mesh in the radial direction to produce a higher-resolution structured mesh near the margin, as shown in Fig. 3. The entire triangular mesh has 5,495 vertices and 10,761 triangles. Its average resolution at the margin is 5 km, whereas in the interior it is about 12 km. Finally, we extrude the two-dimensional mesh in the z-direction through 10 layers to produce a prismatic grid, then cut each prism into three tetrahedra to build the final tetrahedral grid for our three-dimensional computational model. The final grid has 60,445 vertices, 322,830 tetrahedra, and about 1.4 million degrees of freedom.

The overall model time step is limited by the advective CFL condition in the explicit Euler solution scheme for the ice-thickness evolution. We found a time step of 10 years to be adequate for stability in the experiments discussed below. Exps. A, F, and G are run for 100,000 years and Exps. B, C, and D for 60,000 years; all experiments are run to an equilibrium state as indicated by a relatively small change of height, e.g. less than 5e-2 ma^{-1}. For the first time step in each experiment, we first solve with 10 Picard iterations, followed by another 10 Newton iterations, or fewer if the relative residual error which takes the residual of second iteration as initial relative value has decreased to 10^{-12} before the iteration limit is reached. For the remaining time steps, which start with a good initial guess, we first solve with 4 Picard iterations and then continue with another 4 Newton iterations, or fewer if the velocity change (in the maximum norm) is less than 10^{-3} ma^{-1}. The relative residual is used for the initial step because there is no previous velocity to

compare to. On 256 processors, Exps. A, F, and G took about 48 hours to run and Exps. B, C, and D took about 24 hours for our computational model (2000-2500 model years per wall-clock hour). The computational costs for solving the momentum equation, the temperature equation, and the evolution equation at each time step are approximately 13s, 5s, 0.5s at the beginning, and 2.5s, 2.1s, 0.5s when steady state is reached. In the following sections, we discuss additional specifics about the setup and numerical results for each of the experiments. We note that the SIA model results for comparisons are from [25] and that mean values over all SIA models are used; see Tables 4 (Exp. A), 5 (Exp. B), 6 (Exp. C), 7 (Exp. D), and 8 (Exp. G) in [25]. No table was provided there for Exp. F.

4.2.1 Experiment A

In Exp. A, the ice sheet is initiated from no ice on a flat bedrock topography, and evolves over 100,000 years to reach an equilibrium state. The ice-sheet volume, area, and other characteristics at equilibrium are shown in Table 4. The areal extent of the ice sheet is largely controlled by the spatial distribution of accumulation and ablation and is similar for both the SIA and Stokes models. Both the total volume and the divide thickness from the Stokes model is larger than from the SIA model, which means that the ice-sheet shape produced by the Stokes models is bigger. The Stokes results are consistent with a narrow "core" of relatively stiff ice directly beneath the ice divide as originally theorized by [29], later confirmed by observations (e.g., [34]), and discussed in numerous other ice-flow modeling studies (e.g., [9, 18, 26]), i.e., these are accurately described by the Stokes model but cannot be accounted for in SIA models.

Table 4: Results for the EISMINT-II benchmark Exp. A.

	Volume 10^6km^3	Area 10^6km^2	Melt fraction	Divide thickness m	Divide basal temperature K
SIA	2.128	1.034	0.718	3688.342	255.605
Stokes	2.240	1.039	0.796	3776.241	259.914

The basal temperature predicted by the two models is also quite different, although one should note it is already quite different between the different SIA models in [25]. The melt area for the Stokes model is about 7.8% of the basal area, greater than that for the mean of the SIA models and close to the maximum of all SIA models. The divide basal temperature determined by the Stokes model is about 4.3K higher, for reasons similar to those discussed above with respect to the differences in ice-sheet shape. That is, the Stokes model accurately captures the peculiar dynamics beneath flow divides, where deviatoric stresses are abnormally low due to the lack of vertical shear stress. The result is less vertical advection beneath the divide relative to locations just off the divide, relatively less advective cooling beneath the divide, and consequently, a local "hot spot"

beneath the divide. Such hot spots have been discussed previously in the context of ice flow modeling; see, e.g., [10,22,26]. Visual results of Exp. A are presented in the first row of Fig. 4. The hot spots discussed above can be clearly seen in the middle panels. Also, the radial symmetry of the basal temperature is retained by our model; the temperature distribution is smooth and regular in appearance with no cold-ice spokes between the frozen and melted regions of the bed. This is one of the major differences in the results obtained using our Stokes model and previous studies that used SIA models, i.e., for this experiment, most SIA models exhibit cold spokes whereas our Stokes model does not.

4.2.2 Experiment B

Exp. B starts from the final, steady-state result of Exp. A and applies an instantaneous, uniform 5K warming at the surface by changing T_{min} in (4.2) to 243.15 K. Thus, this experiment demonstrates the model response to a step increase in the surface temperature. Table 5 shows the equilibrium change in model characteristics caused by the warming. The warming leads to an increase in divide basal temperatures of nearly 4.59 K, an expansion of the area of basal melt by 7.59%, and a general thinning of the ice-sheet (4.5% at the divide and 2.7% globally).

Table 5: Results for the EISMINT-II benchmark Exp. B.

Changes in	Volume	Melt fraction	Divide thickness	Divide basal temperature
	%	%	%	K
SIA	-2.589	11.836	-4.927	4.623
Stokes	-2.735	7.590	-4.491	4.588

The changes predicted by the SIA models are generally larger that those predicted by the Stokes model; the differences for the changes in the melt fraction and divide thickness are significant. For this experiment, most of the SIA models achieve a new steady state that is radially symmetric with no cold spokes. The Stokes model output is still radially symmetric and regular as is shown in the second row of Fig. 4.

4.2.3 Experiment C

Exp. C starts from the final, steady-state conditions of Exp. A and applies and instantaneous reduction in the local accumulation by reducing M_{max} in (4.1) to 0.25 ma^{-1} and R_{el} to 425 km. This experiment demonstrates the model response to a step accumulation-rate decrease by uniformly reducing the accumulation rate by 0.25 ma^{-1} and by reducing the size of the accumulation area radius by 25 km. Table 6 shows the equilibrium change in model characteristics caused by the reductions in the accumulation rate and the accumulation area. The change leads to a general thinning of the ice sheet (13.1% at divide and 28.3% globally). The divide basal temperature warms by 1.94 K because of the reduction in vertical advection of cold surface ice. Although the reduced height causes the bed at
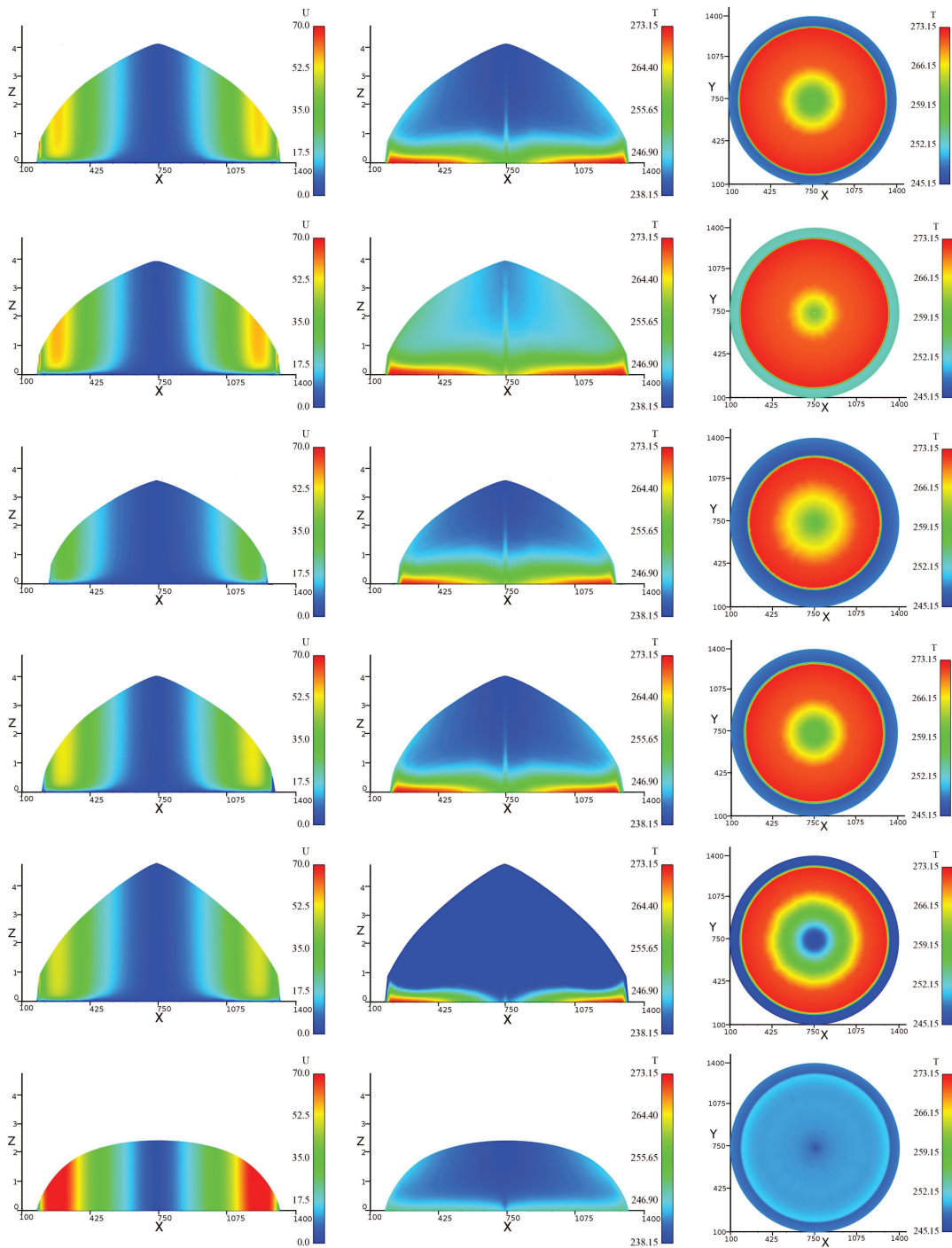
Figure 4: Steady state results for the EISMINT-II experiments from our computational Stokes model. From left to right: the velocity magnitude on the xz-plane, the temperature (K) on the xz-plane, and the basal temperature on the xy-plane. From top to bottom: Exps. A, B, C, D, F, and G.

Table 6: Results of the EISMINT-II benchmark Exp. C.

Changes in	Volume	Area	Melt fraction	Divide thickness	Divide basal temperature
	%	%	%	%	K
SIA	-28.507	-19.515	-27.806	-12.929	3.707
Stokes	-28.315	-19.272	-22.860	-13.128	1.936

the ice-sheet center to be warmer due to advection and diffusion, the melt fraction actually decreases by 22.9% because the thickness over the rest of the ice sheet goes down as well, leading to less insulation of the bed.

The changes predicted by the SIA and Stokes models are similar, except for the divide basal temperature which is significantly smaller for the Stokes model. For this experiment, the SIA models show a considerably reduction in cold-ice spokes compared to Exp. A. The Stokes model again is radial symmetric and regular as shown in the third row of Fig. 4.

4.2.4   Experiment D

Exp. D also starts from the final, steady-state conditions of Exp. A and reduces R_{el} to 425km in (4.1). This experiment demonstrates the model response to a change in the area of accumulation only. Table 7 shows the resulting equilibrium changes in model characteristics. Compared to Exp. C, the change leads to less thinning of the ice-sheet (2.3% at divide and 11.8% globally). The divide basal temperature drops by about 0.22 K because of a reduction in thermal insulation, resulting from a reduction in ice thickness which is not compensated for by a commensurate reduction in vertical advective cooling. The change in melt fraction decreases by only 0.4%.

Table 7: Results of the EISMINT-II benchmark Exp. D.

Change in	Volume	Area	Melt fraction	Divide thickness	Divide basal temperature
	%	%	%	%	K
SIA	-12.085	-9.489	-1.613	-2.181	-0.188
Stokes	-11.836	-9.170	-0.366	-2.343	-0.222

The changes predicted by the SIA and Stokes models are again similar, except for the melt fraction and the divide basal temperatures. For this case, however, SIA models consistently show a steady-state pattern of the basal temperatures that contain cold-ice spokes, similar to those seen in Exp. A. The Stokes model is again radially symmetric and regular, as is shown in the fourth row of Fig. 4.

4.2.5 Experiment F

Exp. F starts with no ice and differs from Exp. A only in that the upper-surface temperature is 15K cooler. The results for Exp. F are given in Table 8. The detailed SIA model results of Exp. F are not provided in [25] (partially because they differ too much between the SIA models) and so we do not include them here. Compared to Exp. A, Exp. F shows that the cooling at the surface leads to a drop in divide basal temperatures of nearly 14 K, a contraction of the area of basal melt by 8.76% of the basal area, and a general thickening of the ice; the divide thickness increases by 465 m and the volume of the ice sheet increases by 1.63×10^5 km^3. For the Stokes model, the symmetry and regularity of all fields is again evident as shown in the fifth row of Fig. 4.

Table 8: Results for the EISMINT-II benchmark Exp. F.

	Volume 10^6km^3	Area 10^6km^2	Melt fraction	Divide thickness m	Divide basal temperature K
Stokes	2.470	1.039	0.4917	4370.936	246.555

4.2.6 Experiment G

Exp. G also starts with no ice and differs from Exp. A in that a sliding basal boundary condition (2.9) is applied on the whole of the bottom bedrock surface. The sliding parameter in that equation is set to $\beta^2 = 1000$ Pa a m^{-1}. Note that the boundary condition (2.9) is different from the SIA boundary condition for which the local basal traction is only the result of the local gravitational driving stress. This experiment demonstrates model behavior under conditions of basal slip.

Table 9 summarizes changes in equilibrium model characteristics for Exp. G. Basal sliding leads to substantial thinning compared to the zero-slip basal velocity condition of Exp. A; there is a 1565 m reduction in the divide height and the volume decreases by 7.25×10^5 km^3. The entire basal area is frozen and the basal temperature at the divide decreases by 14.74 K. This dramatic change occurs because, over the course of the model run, cold ice from the surface is rapidly advected to the ice sheet base as a result of the large ice-flux divergence that accompanies fast basal sliding. The results show fast basal

Table 9: Results of the EISMINT-II benchmark Exp. G.

	Volume 10^6km^3	Area 10^6km^2	Melt fraction	Divide thickness m	Divide basal temperature K
SIA	1.589	1.032	0.353	2365.206	249.134
Stokes	1.514	1.041	0.000	2210.758	245.173

sliding while the entire basal area is frozen because the experiment allows basal sliding to occur regardless of whether or not the basal temperature is at the pressure melting point.

SIA models still produce basal melting; this is a major difference between the SIA and Stokes model results for Exp. G. The Stokes model again is radial symmetric and regular as is shown in the last row of Fig. 4.

4.2.7   On the cold spoke instability

The instability of the SIA models that result in "cold spokes" is discussed in [24,25,30] and elsewhere. At lower surface temperatures, the cold spokes instability of the SIA models becomes more evident; all SIA models discussed in [25] displayed broken symmetry and some, i.e., Exps. A, C, D, and F, developed cold spokes within the basal melting zone. Because of the coupling between the temperature, the deformation rate factor, and the velocity, irregularities eventually propagated into the flow field and the shape of the ice sheet as well. Among all of the EISMINT-II experiments conducted using SIA models, the cold spoke instability is most evident in Exp. F. Fig. 5 shows the simulated steady-stated basal temperatures for Exp. F using the SIA dynamical core in the Community Ice Sheet Model (CISM) [27] on a structured 60×60 grid (grid size 25 km), where cold ice spokes are clearly evident.

To demonstrate that the lack of a cold-spoke instability in our Stokes-model results is not affected by the structure or resolution of the computational grid, we run the Stokes model on Exp. F again but on a structured, three-dimensional grid of horizontal resolution 60×60 (the same grid size as the SIA run of Fig. 5) and 10 vertical layers. The results of the steady state of the ice-sheet are shown in Table 10 and Fig. 6, which are quite close to those obtained on the unstructured grid (Table 8 and the fifth row of Fig. 4). No cold-ice spokes appear in the simulated basal temperature field, as demonstrated by Fig. 6.

Table 10: Results of the EISMINT-II benchmark Exp. F on the structured grid.

	Volume 10^6km^3	Area 10^6km^2	Melt fraction	Divide thickness m	Divide basal temperature K
Stokes	2.637	1.027	0.5106	4468.166	243.724

5   Concluding remarks

We have developed a higher-order discretization accuracy, variable grid resolution capability for simulating the three-dimensional, thermo-mechanical behavior of ice sheets and glaciers based on a dynamical core that couples the nonlinear Stokes equations, the temperature evolution equation, and the mass conservation equation. The high accuracy and stability resulting from the use of quadratic finite elements for the velocity and cubic
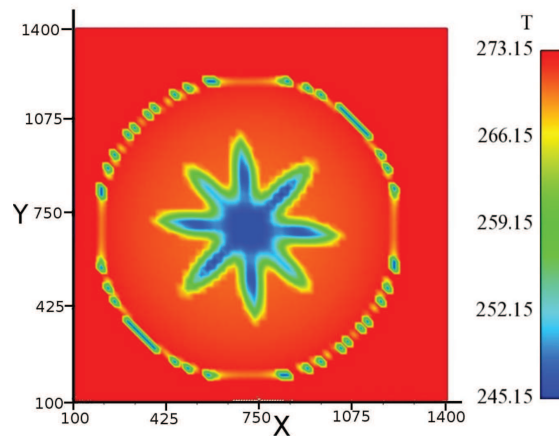
Figure 5: Simulation result of the basal temperature on the xy-plane of the steady states of the EISMINT-II benchmark Exp. F. by the SIA ice dynamical core in the Community Ice Sheet Model (CISM).
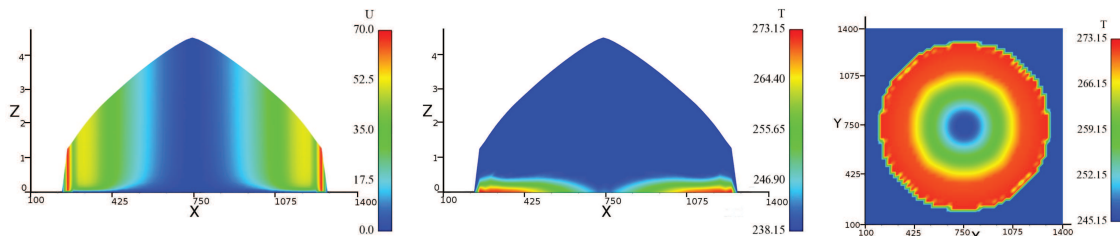

Figure 6: Simulation results of the steady state of the EISMINT-II benchmark experiments F on the structured grid. From left to right: the velocity magnitude on the xz-plane, the temperature on the xz-plane, and the basal temperature on the xy-plane.

finite elements for the temperature is demonstrated. The nonlinear equations are solved using a hybrid Picard-Newton solver, which reduces the number of iterations needed for convergence when compared to the Picard solver alone. Differences in the cost per iteration of the two methods are not significant, and so the hybrid approach results in a considerable reduction in computational cost. The coupled model we have developed can be applied to large-scale problems, such as high-spatial resolution simulations of the Greenland ice sheet, and is stable and accurate over very long time integrations (hundreds of thousands of years).

When applying our model to the EISMINT II experiments for thermo-mechanical ice sheet evolution, we find no evidence for the cold spoke instabilities seen by other authors who have used lower-order approximations to Stokes dynamics (e.g., shallow ice or first-order approximations), uniform grids, and finite difference discretizations. Which aspect or aspects of our methodology is responsible for the elimination of the cold spoke instabilities is unclear. Here, we speculate that the use of a uniform grid alone is not responsible for the instability, as discussed and demonstrated above (e.g., Fig. 6). While

recent work on these same experiments using a first-order approximation to the Stokes equations and finite element methods on an unstructured mesh [5] shows an apparent reduction in the severity of cold spokes, they are not unequivocally absent, nor are the basal temperature fields obviously smooth and symmetric, as in the present work. Based on these observations, we speculate that the finite element method alone is not responsible for removing the instability in our experiments. Exactly which combination of factors from the current model are responsible for removing the instability remains uncertain, and we leave the answer to that question to future work. By using identical grids and discretizations schemes for all the choices of models (e.g., shallow ice, first-order, and Stokes for the dynamics, low-order or higher-order accurate schemes for the temperature evolution, etc.), we should be able to unequivocally answer the question of what causes the cold spoke instability and what combination of models and numerical considerations are required to remove it.

Acknowledgments

References

[1] R.B. Alley and I. Joughin, Modeling Ice-Sheet Flow, Science, 336 (2012), 551-552.
[2] R.B. Alley, P.U. Clark, P. Huybrechts, P., and I. Joughin, Ice sheet and sea-level changes, Science, 310 (2005), 456-460.
[3] J.L. Bamber, R.B. Alley, and I. Joughin, Rapid response of modern day ice sheets to external forcing, Earth Planet Sci. Lett., 257 (2007), 1-13.
[4] D.B. Bahr, Analytical modeling of glacier dynamics, Math. Geology, 28 (1996), 229-251.
[5] D.J. Brinkerhoff and J.V. Johnson, Data assimilation and prognostic whole ice-sheet modelling with the variationally derived, higher-order, open source, and fully parallel ice sheet model VarGlaS, The Cryosphere, 7 (2013), 1161-1184.
[6] A.N. Brooks and T. Hughes, Streamline upwind/Petrov-Galerkin formulations for advection dominated flows, Proc Inter. Conf. on Finite Element Methods in Fluid Flow, Banff, Canada, 1980.
[7] E. Bueler, J. Brown, and C.S. Lingle, Exact solutions to the thermomechanically coupled shallow-ice approximation: effective tools for verification, J. Glaciol., 53 (2007), 499-516.
[8] C. Burstedde, O. Ghattas, G. Stadler, T. Tu, and L.C. Wilcox, Parallel scalable adjoint-based adaptive solution of variable-viscosity Stokes flow problems, Comput. Methods Appl. Mech. Engrg., 198 (2009), 1691-1700.

 [9] M. Carlos, G. H. Gudmundsson, H. D. Pritchard, and O. Gagliardini, On the effects of anisotropic rheology on ice flow, internal structure, and the age-depth relationship at ice divides, J. Geophys. Res., 114 (2009), F04001.

[10] D. Dahl-Jensen, Steady thermomechanical flow along two-dimensional flow lines in large grounded ice sheets, J. Geophys. Res., 94 (1989), B8, 10355-10362.

[11] J.K. Dukowicz, S. Price, and W. Lipscomb, Consistent approximations and boundary conditions for ice-sheet dynamics from a principle of least action, J. Glaciol., 56 (2010), 480-496.

[12] L. Ju, Conforming centroidal Voronoi Delaunay triangulation for quality mesh generation, Inter. J. Numer. Anal. Model., 4 (2007), pp. 531-547.

[13] E. Larour, H. Seroussi, M. Morlighem, and E. Rignot, Continental scale, high order, high spatial resolution, ice sheet modeling using the Ice Sheet System Model (ISSM), J. Geophys. Res., 117 (2012), F01022, doi:10.1029/2011JF002140.

[14] W. Leng, L. Ju, M. Gunzburger, S. Price, and T. Ringler, A parallel high-order accurate finite element Stokes ice sheet model. J. Geophys. Res., 117 (2012), F01001, doi:10.1029/2011JF001962.

[15] W. Leng, L. Ju, M. Gunzburger, and S. Price, Manufactured solutions and the verification of three-dimensional Stokes ice-sheet models, The Cryosphere, 7 (2013), pp. 19-29.

[16] E. Le Meur, O. Gagliardini, T. Zwinger, and J. Ruokolainen, Glacier flow modelling: A comparison of the shallow ice approximation and the full-Stokes solution, Comptes Rendus Physique, 5(7) (2004), 709-722.

[17] M. Morlighem, E. Rignot, H. Seroussi, E. Larour, H.B. Dhia, and D. Aubry, Spatial patterns of basal drag inferred using control methods for a full-Stokes and simpler models for Pine Island Glacier, West Antarctica, J. Geophys. Res., 37 (2010), L14502, doi:10.1029/2010GL043853.

[18] N.A. Nereson, C. F. Raymond, E. D. Waddington, and R. W. Jacobel, Migration of the Siple Dome ice divide, West Antarctica, J. Glaciol., 44 (1998), 643-652.

[19] J. Nye, The distribution of stress and velocity in glaciers and ice-sheets, Proc. R. Soc. London, Ser. A, 239 (1957), 113-133.

[20] W.S.B. Paterson and W.F. Budd, Flow parameters for ice sheet modelling, Cold Reg. Sci. Technol., 6 (1982), 175-177.

[21] W.S.B Paterson, The Physics of Glaciers, Elsevier Science, Oxford, U. K, 1994.

[22] F. Pattyn, A new 3D higher-order thermomechanical ice-sheet model: Basic sensitivity, ice-stream development and ice flow across subglacial lakes, J. Geophys. Res., 108(B8) (2003), 2382, doi:10.1029/2002JB002329.

[23] F. Pattyn, L. Perichon, A. Aschwanden, B. Breuer, D.B. Smedt, O. Gagliardini, G.H. Gudmundsson, R.C.A. Hindmarsh, A. Hubbard, J.V. Johnson, T. Kleiner, Y. Konovalov, C. Martin, A.J. Payne, D. Pollard, S. Price, M. Ruckamp, F. Saito, S. Sugiyama, S., and T. Zwinger, Benchmark experiments for higher-order and full-Stokes ice sheet models (ISMIP-HOM), The Cryosphere, 2 (2008), 95-108.

[24] A.J. Payne and D.J. Baldwin, Analysis of ice-flow instabilities identified in the EISMINT intercomparison exercise, Annals of Glaciology, 30 (2000), 204-210.

[25] A.J. Payne, P. Huybrechts, A. Abe-Ouchi, R. Calov, J.L. Fastook, R. Greve, S.J. Marshall, I. Marsiat, C. Ritz, L. Tarasov, and M.P.A. Thomassen, Results from the EISMINT model intercomparison: the effects of thermomechanical coupling, J. Glaciol., 46 (2000), 227-238.

[26] S. Price, H. Conway, and E.D. Waddington, A full-stress, thermomechanical flow band model using the finite volume method, J. Geophys. Res., 112 (2007), F03021, doi:10.1029/2006JF000725.

[27] I.C. Rutt, M. Hagdorn, N.R.J. Hulton, and A.J. Payne, The Glimmer community ice sheet model, J. Geophys. Res., 114 (2009), F02004.
[28] S.R. Shannon, A.J. Payne, I.D. Bartholomew, M.R. van den Broeke, T.L. Edwards, X. Fettweis, O. Gagliardini, F. Gillet-Chaulet, H. Goelzer, M.J. Hoffman, P. Huybrechts, D. Mair, P. Nienow, M. Perego, S.F. Price, C.J.P. Smeets, A.J. Sole, R.S.W. van de Wal, and T. Zwinger, Enhanced basal lubrication and contribution of the Greenland ice sheet to future sea-level rise, PNAS, in press (2013), doi: 10.1073/pnas.1212647110.
[29] C.F. Raymond, Deformation in the vicinity of ice divides, J. Glaciol., 29 (1983), 357-373.
[30] F. Saito, A. Abe-Ouchi, and H. Blatter, European Ice Sheet Modelling Initiative (EISMINT) model intercomparison experiments with first-order mechanics. J. Geophys. Res., 111(F2) (2006), F02012.
[31] C. Schoof and R.C.A. Hindmarsh, Thin-Film Flows with Wall Slip: An Asymptotic Analysis of Higher Order Glacier Flow Models, Quarterly J. Mech. & App. Math., 63(1) (2010), 73-114.
[32] S. Solomon, D. Qin, M. Manning, Z. Chen, M. Marquis, K.B. Averyt, M.Tignor, and H.L. Miller (eds.), Climate Change 2007: The Physical Science Basis. Contribution of Working Group I to the Fourth Assessment Report of the Intergovernmental Panel on Climate Change, Cambridge University Press, Cambridge, United Kingdom and New York, NY, USA, 2007.
[33] T.F. Stocker, D. Qin, G.-K. Plattner, M. Tignor, S. K. Allen, J. Boschung, A. Nauels, Y. Xia, V. Bex, and P.M. Midgley (eds.), Climate Change 2013: The Physical Science Basis. Contribution of Working Group I to the Fifth Assessment Report of the Intergovernmental Panel on Climate Change, Cambridge University Press, Cambridge, United Kingdom and New York, NY, USA, 2013.
[34] D.G. Vaughan, H.F.J. Corr, C.S.M. Doake, and E. D. Waddington, Distortion of isochronous layers in ice revealed by ground-penetrating radar, Nature, 398 (1999), 323-326.
[35] H. Zhang, L. Ju, M. Gunzburger, T. Ringler, and S. Price, Coupled models and parallel simulations for three dimensional full-Stokes ice sheet modeling, Numer. Math. Theo. Meth. Appl., 4 (2011), 359-381.
[36] T. Zwinger, R. Greve, O. Gagliardini, T. Shiraiwa, and M. Lyly, A full Stokes-flow thermomechanical model for firn and ice applied to the Gorshkov crater glacier, Kamchatka, Ann. Glaciol., 45 (2007), 29-37.